Fused Filament Fabrication-Based Additive Manufacturing of Commercially Pure Titanium

Yvonne Thompson,* Markus Polzer, Joamin Gonzalez-Gutierrez, Olga Kasian, Johannes P. Heckl, Valentin Dalbauer, Christian Kukla, and Peter J. Felfer

Fabrication of titanium components is very cost intensive, partly due to the complex machining and limited recyclability of waste material. For electrochemical applications, the excellent corrosion resistance of pure titanium is of high importance, whereas medium mechanical strength of fabricated parts is sufficient for such a use case. For smaller parts, metal fused filament fabrication (MF^3) enables the fabrication of complex metallic structures densified during a final sintering step. Pure titanium can be processed to near-net-shape geometries for electrochemical applications if the parameters and the atmosphere during sintering are carefully monitored. Herein, the influence of thermal debinding and sintering parameters on the fabrication of high-density pure titanium using MF^3 is investigated. Particular focus is placed on enhancing sintered density while limiting impurity uptake to conserve the high chemical purity of the initial powder material. Relative densities of 95% are repeatedly reached inside the bulk of the samples. An oxygen content of 0.56 wt% as a result of vacuum processing induces the formation of the retained α-Ti phase (925 $HV_{0.2}$) inside the α matrix (295 $HV_{0.2}$). Fabricated parts exhibit high mechanical strength, albeit reduced elongation due to remaining pores, and, in terms of electrochemistry, enhanced stability toward anodic dissolution.

1. Introduction

Titanium and its alloys are interesting for various engineering applications due to their high specific strength, low density, and excellent corrosion resistance. For electrochemical applications, thin titanium structures can be used as gas diffusion backing in polymer electrolyte membrane fuel cells.[1] Near-net-shape forming processes based on powder metallurgy (PM) can substitute the difficulties of conventional machining, save material during fabrication, reduce the variety of stock material that needs to be stored, and contribute to cost reductions.

Among these, powder bed fusion technologies such as selective laser melting (SLM) and electron beam melting (EBM) represent options for additive manufacturing of titanium and titanium alloys to complex components of high density.[2,3] Limitations of these cost-intensive beam-based methods comprise slow deposition rates and relatively small dimensions of the build chambers. Alternatively, for larger structural components, direct energy deposition technologies like wire and arc additive manufacturing (WAAM) of titanium alloys are currently under intensive investigations, especially for aerospace applications.[4,5] In **Figure 1**, the AM methods mentioned earlier are compared with more cost-efficient alternatives,[6] that make use of polymeric binders during shaping and require postprocessing for binder removal and sintering densification of fabricated metal structures. Binder jetting (BJT) with metal powders (MBJT) has been proven successful for functional titanium parts, and commercially available systems enable the fabrication of components

Y. Thompson, M. Polzer, J. P. Heckl, V. Dalbauer, P. J. Felfer
Department of Materials Science and Engineering
Institute I), Friedrich-Alexander-Universität Erlangen-Nürnberg
Martensstraße 5, 91058 Erlangen, Germany
E-mail: yvonne.thompson@fau.de

J. Gonzalez-Gutierrez
Department of Polymer Engineering and Science
Institute of Polymer Processing
Montanuniversitaet Leoben, Otto Gloeckel-Str. 2, 8700 Leoben, Austria

The ORCID identification number(s) for the author(s) of this article can be found under https://doi.org/10.1002/adem.202100380.

O. Kasian
Helmholtz Institut Erlangen-Nürnberg
Helmholtz-Zentrum Berlin GmbH
Hahn-Meitner-Platz 1, 14 109 Berlin

O. Kasian
Department of Materials Science and Engineering
Friedrich-Alexander-Universität Erlangen-Nürnberg
91 058 Erlangen, Germany

C. Kukla
Industrial Liaison Department
Montanuniversitaet Leoben
Peter Tunner Str. 27, 8700 Leoben, Austria

ADVANCED
SCIENCE NEWS
www.advancedsciencenews.com

ADVANCED
ENGINEERING
MATERIALS
www.aem-journal.com
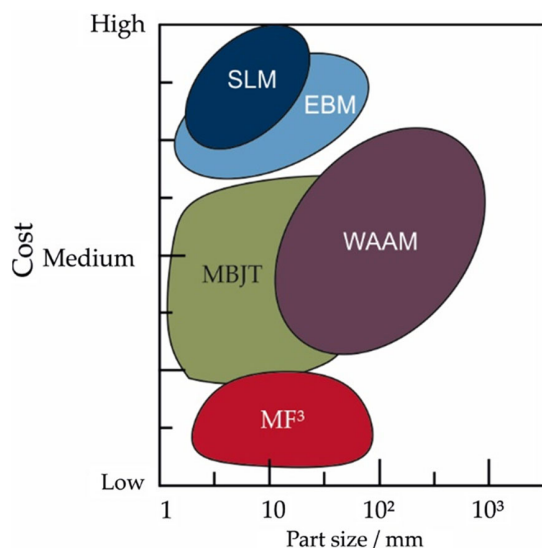
Figure 1. Comparison of key metal additive manufacturing methods in terms of part size and costs. SLM: selective laser melting, EBM: electron beam melting, WAAM: wire and arc additive manufacturing, MBJT: metal binder jetting, and MF³: metal fused filament fabrication.[5–7]

over a wide dimensional range.[7] However, the use of a powder bed limits the maximum packing density of the printed green body, leading to large amounts of remaining porosity after sintering. Here, material extrusion (MEX), as in fused filament fabrication (FFF) of a polymeric filament with a high amount of incorporated titanium powder particles (aka metal FFF or MF³), enhances green-body density and allows for the fabrication of highly dense parts after pressureless sintering. MF³, therefore, is a low-cost fabrication method for small functional components that is successfully applied for the fabrication of titanium alloys.[8–11] To date, however, there has been no study focusing on the processing of pure titanium, where the preservation of chemical purity is the primary concern and absence of alloying elements is required.

The drawback of the two processes that use sintering during the finalizing step (MBJT, MF³) is the high sensitivity of titanium for the uptake of interstitial elements, which can be detrimental to the mechanical properties of the final products.[1,9] In particular, high levels of oxygen can be present already after powder production and increase even more during sintering. Thus, a trade-off between cost-efficient fabrication and fulfillment of property requirements must be found for specific application cases.

In electrochemical applications, titanium, with its high corrosion resistance, is required to constitute thin and porous plates in anodic parts of electrolysis cells. If unalloyed commercially pure (CP) titanium powder, as defined by the ASTM F67,[12] that only contains minimal amounts of interstitial elements, is used in the MF³ process, it can serve as an economical technology for the fabrication of titanium structures. The thermal debinding and sintering parameters have to be carefully controlled to conserve the original high purity of titanium. Thermal debinding for thorough binder removal must deliver defect-free parts with minimal levels of residual carbon. Otherwise, insufficient binder removal can

create increased carbon content and lead to severe degradation of mechanical properties.[13,14] Subsequent sintering is used to densify the brown bodies and must be adapted to the specific material and furnace setup to create the highest densities achievable.
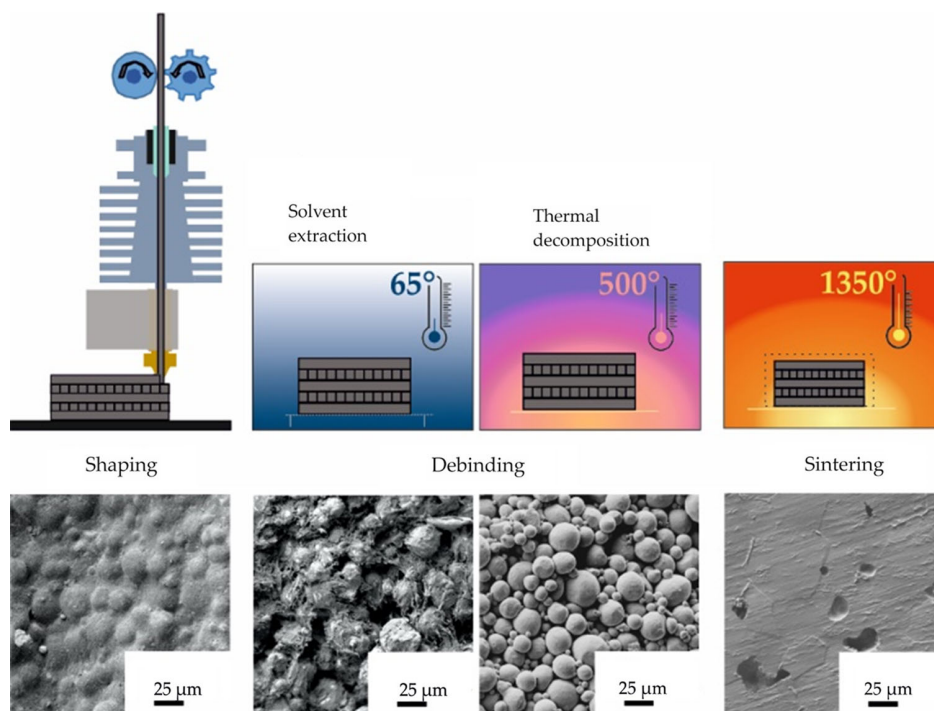
Several studies have been reported for sintering of titanium in the literature to reach optimized densification without application of external pressure during processing.[15–17] Generally, the activation energy for self-diffusion of titanium is lower in the β-Ti range above 882 °C, leading to accelerated densification at temperatures above the α→β transformation. Attempts have been made to take advantage of the α→β transformation by cyclically heating around the transformation temperature to generate enhanced sintering. Indeed, it was shown that the α→β transformation increases the sintering rate, whereas the reverse transformation has little effect.[15] Apart from the thermal conditions, the atmospheres also have a significant impact on sintering behavior. Like other metal powders, titanium particles are enveloped with an oxide film.

While persistent oxide films disable the sintering of powder particles, in the case of titanium, the oxide films are not persistent at elevated temperatures because of the significant solubility of oxygen in both α-Ti and β-Ti.[16] Nevertheless, dissolved oxygen inside the sintered titanium forms an interstitial solid solution and leads to a significant increase in strength, hardness, and brittleness.[18] Therefore, controlling oxygen in the sintering atmosphere is indispensable to reducing impurity uptake into the bulk material. Besides using argon gas or high vacuum levels of 10^{-7} mbar or better, some studies suggest thermohydrogen processing for finer grains and better densification.[17,19] In any case, as-sintered CP Ti is usually not a single-phase material. This microstructure is caused by iron impurities, leading to the formation of iron-enriched grain boundary (GB) phases during cooling at the end of the sintering cycle. The fast diffusion of Fe toward the grain boundaries triggers the generation of β-Ti GB phases.[20]

In this study, the MF³ process was applied to manufacture CP titanium, as shown in **Figure 2**, following a shaping, debinding, and sintering (SDS) processing path.

A composite of 55 vol% titanium powder and a novel binder system, consisting of a blend of thermoplastics and additives, was compounded, and homogenous filaments were extruded. These highly filled filaments are processable in any commercial FFF printer. Previous studies have proven the applicability of the used binder system for additive manufacturing of alumina, cermets, neodymium−iron−boron alloy, and steels.[21–25] After the shaping by FFF, the binder is removed, partially by solvent extraction and finally by thermal degradation. Full densification is obtained by sintering, resulting in relative pore volumes of less than 5%. Figure 2 shows the respective microstructure during each of the CP titanium processing steps and is discussed in detail in Results.

In this study, MF³ was studied as a low-cost AM method for functional titanium parts with high density and low impurity levels. Different atmospheres for thermal debinding and sintering were investigated, and, in each case, the temperature program was optimized concerning the highest resulting density. The remaining oxygen and carbon contents were measured using hot gas extraction, and the resulting microstructures were

**ADVANCED
SCIENCE NEWS**
www.advancedsciencenews.com

*ADVANCED
ENGINEERING
MATERIALS*
www.aem-journal.com

Figure 2. Schematic representation and microstructure evolution during the SDS process.

analyzed using scanning electron microscopy (SEM). For mechanical characterization, hardness measurements from the surface into the bulk material were carried out. Microtensile tests were applied for further mechanical characterization, as the dimensions of the tube furnace used in this project restricted the sample dimensions and the size for standard ISO 6892-1 tensile tests could not be fitted in the furnace.

2. Experimental Section

2.1. Materials

The highly filled filament used in this study consisted of 55 vol% CP titanium powder (TLS Technik GmbH & Co. Spezialpulver KG, Germany) and a polymeric binder system (Institute of Polymer Processing, Montanuniversitaet Leoben, Austria). The used powder was produced by gas atomization, which resulted in spherical particle shape, as shown in the SEM images in **Figure 3**a. The particle size distribution of the titanium powder was analyzed using optical particle size analysis (Camsizer XT, Retsch Technology, Germany). Figure 3b shows the measurement results in the form of the relative fraction of particles within the determined size classes of the 2 μm range and the cumulative fraction of particle size. The mean particle value was thereby determined to be 23.4 μm. Particles were embedded as shown in Figure 3d into a multicomponent confidential binder available at the Institute of Polymer Processing (Montanuniversitaet Leoben, Austria).[26]

   The binder system consisted of two ingredients; one of them provided mechanical flexibility and the other stiffness, necessary to unspool and feed the highly filled filament to the printing head

without the risk of breakage. The major fraction of the binder was a styrene-based thermoplastic elastomer (TPE) (Kraiburg TPE GmbH & Co. KG, Germany) that was soluble in cyclohexane; the second component is an insoluble grafted polyolefin (BYK Chemie GmbH, Germany), which provided stability after solvent extraction of the main component. The feedstock ingredients (binder and Ti powder) were compounded in a corotating twin-screw extruder ZSE 18 HP-48D (Leistritz Extrusionstechnik
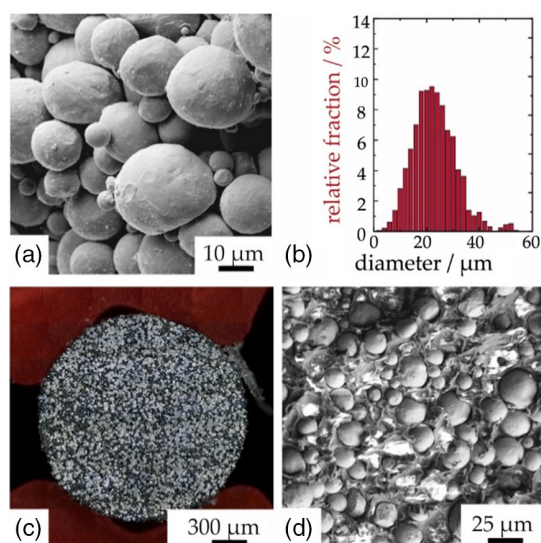
Figure 3. a) Spherical Ti particles as received, b) particle size distribution of Ti powder, c) cross-sectional view of filament containing binder and Ti particles, and d) larger magnification of filament cross section.

2100380 (3 of 12)

GmbH, Germany). The compounder had two gravimetric feeding units containing the binder and Ti powder, respectively. Argon gas was used in the hopper containing Ti powder to minimize oxidation of powder and reduce the risk of fire during compounding. The compounder had 13 heating zones that were set to 25, 180, 180, 190, 200, 200, 200, 200, 200, 200, 200, 200, and 210 °C. The binder was introduced in the zone set at 25 °C to prevent premature melting and good transport of the binder pellets. The Ti powder was introduced at the fourth zone set to 190 °C via a side feeder. The rotational speed of the corotating screws was set to 600 rpm. The die at 210 °C had two round openings of 1.75 mm in diameter. The extrudate was cooled down in a conveyor belt with fans before being pelletized in a strand pelletizer (Reduction Engineering Scheer, USA). The produced pellets were used to produce filaments in an FT-E20T-MP-IS single screw extruder (Dr. Collin GmbH, Germany), as described in the study by Gonzalez-Gutierrez et al.[27] A single screw extruder was used to obtain a constant pressure that allowed reliable extrusion of material, which is critical to obtain filaments with constant dimensions. The extruder barrel had three heating zones set at 180, 190, and 200 °C, starting from the hopper. The die with a round orifice of 1.75 mm in diameter was separately heated to 200 °C. The screw rotational speed was set to 30 rpm. The extruded filament was collected on a conveyor belt and allowed to cool down before it was spooled. The filament diameter and ovality were monitored with a laser micrometer (Sikora AG, Germany) and the haul-off speed and winding speeds were adjusted to obtain filaments with a diameter of 1.75 ± 0.02 mm and ovality of 0.012 ± 0.005 mm.

Image analysis of the filament cross section as shown in Figure 3c was conducted using Image J to quantify the metal content, which was indeed 55 vol.-%. Also, the homogeneity of the particle distribution within the filament was evaluated qualitatively using the same cross-sectional images.

2.2. Shaping

Shaping was realized using a desktop 3D printer, Prusa i3 MK2 fused filament fabrication machine (Prusa Research, Prague, Czech Republic). The printer was equipped as described in the study by Lengauer et al.,[22] having a direct drive extruder with a hardened steel nozzle of 0.6 mm diameter. The slicer program used was Simplify3D (version 3.1.1, Simplify3D, Cincinnati, OH, USA). All parts were printed nominally fully dense, that is, at 100% infill with an alternating rectilinear and concentric infill pattern (Figure 5a). A volumetric flow rate of 25 mm^3 s^{-1} was chosen for a printing speed of 10 mm s^{-1}. All layers were printed with 0.2 mm layer height, extruding 120% of the geometrically necessary material volume ("extrusion multiplier" at 1.2). Nozzle temperature was set to 280 °C, whereas a bed temperature of 80 °C, which was well above the glass transition temperature T_g of the binder components, was used to prevent warpage and achieve best adhesion of the first layer. A self-adhesive polypropylene film was used as a print substrate to enhance the bonding of the first layer to the printing bed.

Samples were designed to fit into a cylinder hot mounting press (LaboPress 1, Struers, Copenhagen, Denmark) to densify the printed green bodies. The diameter of the samples was

therefore set to 25 mm. Printed heights of 4 and 6 mm were used, leading to a compressed height of 3.7 and 5.6 mm, respectively. Pressing of the samples was conducted at 180 °C for 10 min and pressing force was varied between 20 and 50 kN to provide consolidation of printing gaps. The cylinder press served as a proof of concept to enable the application of green-body warm compression with simple means and investigate how isostatic compression in the green state affects the density of the MF^3 component. It allowed the application of quasi-isostatic compression in a laboratory setup, providing green bodies with less printing-induced defects. Alternatively, existing methods that enable true isostatic compression could also be applied to FFF-printed green bodies. These would be, for example, compression with the use of liquids or gas isostatic forging that was already successfully used at higher temperatures for densification of titanium alloys.[19] As the latter processes did not require molds due to the use of liquids or gases, they could also be applied to complex 3D geometries. For debinding and sintering trials, the compressed green bodies were cut into four pieces, enabling the best comparability within the various test batches. Microstructure analysis and atom probe tomography (APT) were conducted on samples compressed in the green state before debinding and sintering. Hardness measurements and corresponding chemical analysis were conducted both on compressed and on noncompressed specimen. For tensile testing, hourglass-shaped specimens in the green-body state were fabricated by milling (Pocket NC V2-10, Bozeman, MT, USA) of the entire printed uncompressed cylinders. Tensile specimens after milling were oversized by 15% in linear dimensions to consider shrinkage during debinding and sintering.

2.3. Debinding

The multicomponent binder system was suitable for a two-step debinding process. During initial solvent debinding, the printed parts were immersed in cyclohexane ($\geq$99.5%, Carl Roth GmbH + Co KG, Karlsruhe, Germany) for chemical extraction of the primary binder polymer (TPE). Weight loss of the samples was monitored, and solvent debinding was considered complete as soon as 98.5 wt% of the total TPE content was removed.

Thermal debinding was conducted by heating in an argon or vacuum furnace before sintering. Depending on the volatilized binder levels, the pressures of the vacuum furnace varied between 10^{-3} and 10^{-5} mbar. In the inert gas furnace case, a continuous argon flow was set to 50 mL min^{-1} and kept constant during the entire process. Debinding temperatures and applicable heating rates were evaluated according to degradation data obtained from thermogravimetric analysis (TGA Q5000, TA Instruments, New Castle, DE, USA). TGA measurements were carried out in nitrogen to obtain representative results for polymer degradation in the oxygen-free environment. Interrupted thermal debinding with recordings of weight loss was used to observe binder burnout in the furnace environment. Stepwise heating schedules were subsequently implemented, which included fast preheating to shorten the total debinding time and slow heating to reduce defect formation in the critical range. The final debinding schedule included slow heating at a rate of 0.2 °C min^{-1} between 170 and 450 °C and was concluded by a

60 min dwell time to allow complete binder evaporation. For reasoning of the selected process parameters, see the elaborations in Section 3.2.
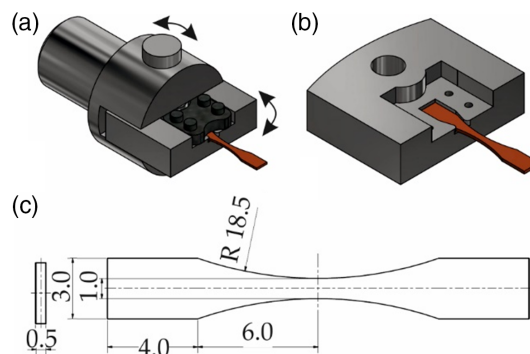
2.4. Sintering

Sintering of the completely debound parts was subsequently conducted in the same vacuum furnace under a pressure of 10^{-4} mbar to prevent oxidation of the titanium particles. Higher vacuum levels could not be realized with the furnace used in this project, which is recommended to enhance sintering densification and microstructural purity and is planned for future studies. Argon sintering was done accordingly with constant gas flow directly after thermal debinding without changing the furnace. Different sintering times (from 90 to 300 min) and temperatures (from 1300 to 1400 °C) were applied in a vacuum to create maximum densification. Slow cooling of 3 °C min^{-1} inside the same furnace was applied in any of the present sintering cycles. After optimizing the sintering program, a holding time of 300 min at 1350 °C was used for the preparation of specimens for mechanical testing. In addition, argon sintering was conducted to compare the influence of different atmospheres on the final density, microstructure, and mechanical properties.

Sintered samples were characterized using backscattered electron (BSE) imaging and energy-dispersive X-ray spectroscopy (EDX) (Zeiss Crossbeam 1540, Carl Zeiss Microscopy GmbH, Jena, Germany) for characterization of the obtained microstructure and nondispersive infrared technology (NDIR) for analysis of carbon and oxygen content (EMIA 320V2 and EMGA 620 WC, Horiba Jobin Yvon, Germany). APT (CAMECA LEAP 4000X HR) for analysis of the GB phase was conducted on tips prepared by focused ion beam (FIB) (Zeiss Crossbeam 540, Carl Zeiss Microscopy GmbH, Jena, Germany) lift-outs of the specific GB and matrix regions. Vickers' hardness of the matrix and different phases was measured for mechanical characterization, according to DIN EN 6507 (HV 0.2), with a load of 1.96 N.

2.5. Tensile Tests

Due to the size limitations of the furnace and cylinder press, no samples big enough for standard ISO 6892-1 tensile tests were fabricated. Therefore, a microtensile test setup (Kammrath & Weiss GmbH, Dortmund, Germany) was used and a clamping system was constructed to ensure gimbal specimen fixation. The tensile module was equipped with a 5 kN load cell. The size and shape of the tested hourglass specimens and the mounting and test setup are shown in **Figure 4**. Specimen geometries were determined so that the stress increase in the gauge length was 200% with respect to the specimen areas being fixated in the clamping system. Accordingly, yielding occurred solely in regions being uninfluenced by fixation. The small overall dimensions of the specimens with a height of 0.5 mm ensured that applied stresses during tensile testing were sufficient to fracture all measured specimens. As specimen sliding in the clamping must be prevented, and fixation areas were small, a combination of force- and form-fitting fixation was chosen. Force fitting was achieved by pressing a roughened bracket on the specimen with miniaturized screws (see Figure 4a), whereas form fitting was

Figure 4. a) Gimbal mounting of the microtensile samples with a rotatable bearing of the slide; b) form fitting of samples into the slide; and c) dimensions of the hourglass samples after sintering.

realized by creating a specimen-shaped cavity in the sample holder using sink erosion (see Figure 4b). Depths of the introduced cavities were designed to align the transversal symmetry axis of the specimen and the testing unit, respectively. In combination with the rotatable bearing of the slide by a connecting rod (Figure 4a), the 2D gimbal fixation of the specimens was realized.

All tensile tests were monitored in situ by digital video microscopy (Keyence VHX-600, Keyence Corporation, Neu-Isenburg, Germany) and elongations during tensile testing were calculated by digital image correlation (Veddac 6.0.1.2, Chemnitzer Werkstoffmechanik GmbH, Chemnitz, Germany) according to regions of highest strain.

Samples were printed as described in Section 2.2; the shape of the tensile specimen was then obtained by milling in a greenbody state. Afterward, debinding and sintering were conducted with the optimized sintering duration of 300 min at a peak sintering temperature of 1350 °C according to the results presented in Section 3.3. The samples were constructed oversized by 15% in linear dimensions to compensate for the linear shrinkage of the samples during sintering.

The sintered samples were cut horizontally and ground to have a thickness of 0.5 mm. Microtensile tests were conducted at a velocity of 5 μm s^{-1} until breakage.

2.6. Electrochemical Measurements

The electrochemical stability tests of as-sintered samples were conducted using the scanning flow cell (SFC)−inductively coupled plasma mass spectrometer (ICP-MS, NexION 350X, Perkin Elmer)-based setup, described in detail in the study by Topalove et al.[28] All presented data were normalized to the geometric area of the working electrode, defined by the size of the flow cell opening ($\approx 1 \times 10^{-2}$ cm^2). A graphite rod placed in the inlet channel of the SFC was used as the counterelectrode. A commercial Ag/AgCl/3M KCl electrode (Metrohm, Germany) was used as the reference electrode. All potentials reported in the manuscript are presented versus the reversible hydrogen electrode (RHE) scale. All electrochemical measurements were carried out in an Ar-saturated 0.1 M HClO$_4$ solution prepared by dilution of concentrated perchloric acid (Suprapur 96%, Merck, Germany)

**ADVANCED
SCIENCE NEWS**
www.advancedsciencenews.com

**ADVANCED
ENGINEERING
MATERIALS**
www.aem-journal.com

in ultrapure water (PureLabPlus system, Elga, 18 Mcm, TOC < 3 ppb). The electrolyte flow rate was kept constant at ≈196 μL min^{-1}. Downstream of the electrochemical cell and prior to introduction into the ICP−MS, the electrolyte was mixed with an internal standard (mixing ratio 1:1). For the detection of the ^{55}Ti isotope, the isotope of ^{50}Sc was used. The concentration of the internal standard in the solution was 10 μg L^{-1}. Calibration of ICP−MS was conducted on each experiment the day before electrochemical measurements. The potentiostat Gamry Reference 600 (Warminster, PA, USA) was used for electrochemical measurements. First, the working electrodes were held at the open-circuit potential (OCP) to estimate the initial dissolution of Ti. Afterward, the potential was swept from $E = 1.25$ V$_{RHE}$ to a value corresponding to a current density of $j = 1$ mA cm^{-2} with a scan rate of 10 mV s^{-1}. At least three measurements were carried out for each spot of the same composition to ensure the reproducibility of the results. As a benchmark material, 0.5 mm Ti foil (99.99%, Sigma Aldrich) was used.

3. Results and Discussion

Parameter optimization of all SDS process steps was conducted to obtain the highest sintering density of the additively fabricated titanium parts. Print settings were adjusted to create nominally dense green bodies, and subsequent warm pressing was studied to remove minor remaining gaps between printed strands and provide additional densification of green bodies. After verification of complete solvent debinding, the thermal debinding step

was investigated to implement a stepwise heating program for thorough binder removal without blister formation at the shortest duration possible. Sintering to the highest density was realized by optimizing the sintering temperature and time in a vacuum.

3.1. Shaping

Printing trials at different nozzle temperatures, all above the melting temperature of the binder polymer of 220 °C, revealed that 280 °C is most appropriate for the continuous extrusion of the highly filled filament at controlled flow rates. To reduce the formation of voids, alternating rectilinear and concentric infill patterns were chosen, as shown in **Figure 5**a. As the green bodies still revealed some remaining porosities attributable to printing defects and poor bonding between adjacent printed layers, a warm pressing step was added for additional densification and void closure. A cylinder press was used at 180 °C, and best consolidation of printing gaps could be obtained by applying a force of 45 kN corresponding to 92 MPa for 10 min. After compression, the relative density of green bodies was increased by $0.5 \pm 0.08\%$, leading to a relative increase in sintered density above $1 \pm 0.37\%$. The main benefit of the compression step lies in reducing the standard deviation of the green-body density. An additional positive side effect is the correction of warpage and the reduction of surface roughness, resulting from the printing process. Therefore, compression of green bodies helps reduce minor printing defects; eliminating pores that would otherwise remain even after the sintering step (see Figure 5c).
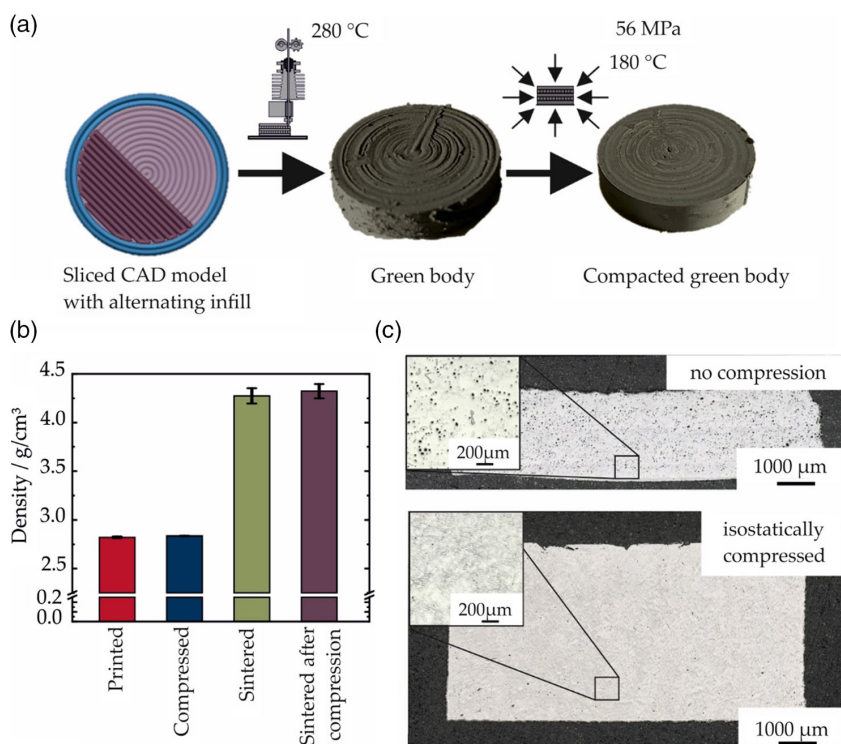
Figure 5. a) Schematic representation of the process routing: computer aided design (CAD) modeling shaping via FFF and compression of green bodies. b) Density of samples after printing, compression, and sintering. c) Overview of sintered samples, without compression (above) and with compression.

**ADVANCED
SCIENCE NEWS**
www.advancedsciencenews.com

**ADVANCED
ENGINEERING
MATERIALS**
www.aem-journal.com

3.2. Debinding

All samples were solvent debound with the removal of at least 98.5 wt% of the primary binder polymer. TGA was conducted in nitrogen at a heating rate of $5\,°C\,min^{-1}$ to study the degradation of the backbone polymer in an oxygen-free environment. Debinding experiments, as described in a previous study,[24] have shown that the printed samples require slower heating to avoid blister formation during polymer degradation and outgassing. Therefore, the degradation values at a rate of $0.2\,°C\,min^{-1}$ (red dashed graph in **Figure 6**) were calculated based on the measured TGA data.

Interrupted thermal debinding tests were conducted to evaluate the actual degradation behavior of the backbone polymer in the used vacuum furnace. The blue squares in Figure 6 indicate the remaining weight percentage of backbone polymer after heating to the indicated temperature with $0.2\,°C\,min^{-1}$. Cooling was done at $5\,°C\,min^{-1}$ directly after reaching the respective temperature. According to the remaining sample weight, the recorded polymer removal correlates very well with the TGA data obtained (Figure 6).

Partially debound samples were manually bent until fracture, and SEM images of the internal fracture surfaces were used to observe the development of the microstructure during ongoing thermal debinding. Directly after printing, the green body consists of titanium particles that are embedded into the polymeric binder. The initial condition for thermal debinding is obtained after solvent debinding and is distinguished by interconnected pore channels inside the green body, as shown in the left SEM image in Figure 6. Titanium particles are in this stage still entirely enveloped into the fibrous network of the backbone polymer. At 350 and 375 °C, first, microstructural changes become visible as the amount of polymer is progressively reduced. Particles are still kept in place by the remaining polymer. The stability of the samples is in that state noticeably reduced, as porosity emerging from the removed binder is increased. At 400 °C, almost all polymer is removed, and in the presintered state at 650 °C particles are clearly rearranged and packed more densely.

A stepwise heating program was developed using the acquired information to implement defect-free thermal debinding at the shortest possible time. The heating rate was markedly reduced in the critical range within 300 and 450 °C to account for binder degradation and give time for evaporation of degradation products through the pore channels. Nevertheless, debinding tests revealed blister formation at temperatures below 300 °C when heating in vacuum at $1\,°C\,min^{-1}$. This blistering is probably related to the volume expansion of the binder when reaching and exceeding the melting temperature of the backbone polymer. Therefore the final temperature program includes slow heating starting from 170 °C to account for volume changes. An additional 60 min dwell time was incorporated after reaching 450 °C to allow complete polymer removal before the onset of sintering and pore closure.
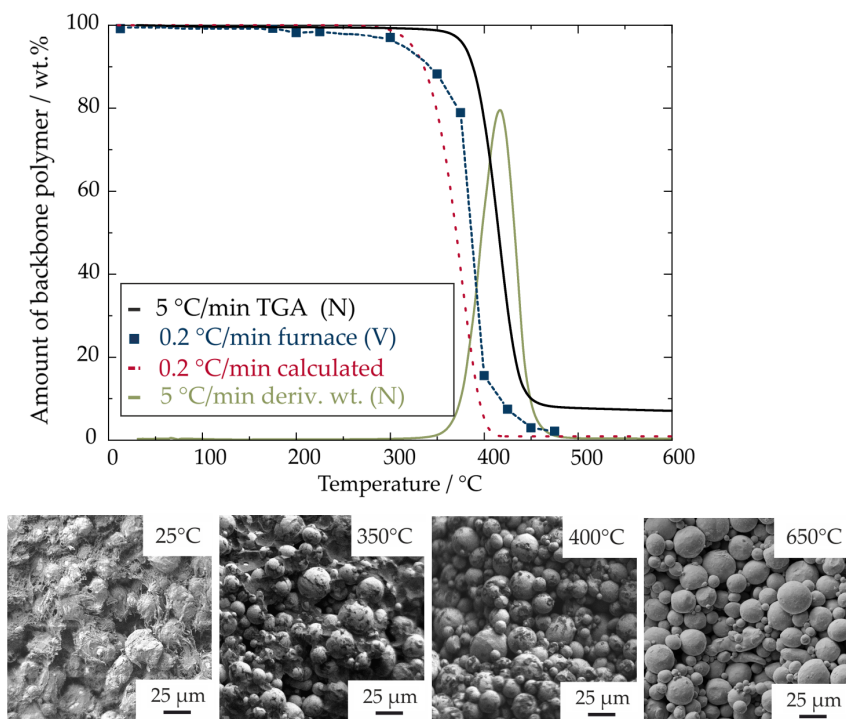
Figure 6. Degradation of the backbone polymer measured in controlled N$_2$ atmosphere at $5\,°C\,min^{-1}$, calculated for a heating rate of $0.2\,°C\,min^{-1}$ (red dotted line) and measured by interrupted thermal debinding at $0.2\,°C\,min^{-1}$ in a vacuum furnace (blue squares). The green line gives the weight derivative curve measured at $5\,°C\,min^{-1}$ in N. Representative microstructures at the various stages of thermal debinding show the removal of the backbone polymer and particle rearrangements.

**ADVANCED
SCIENCE NEWS**

www.advancedsciencenews.com

**ADVANCED
ENGINEERING
MATERIALS**

www.aem-journal.com

Table 1. Relative sintered densities in the percentage of the TD of $4.5\,g\,cm^{-3}$ of bulk titanium after sintering at the indicated temperatures and times.

Relative sintered density in percent of the theoretical density of $4.5\,g\,cm^{-3}$				
Time in min Temperature in °C	90	120	210	300
1300	89.97	–	–	–
1350	89.68	88.91	93.07	93.16
1400	91.87	–	–	–

3.3. Sintering

Sintering times and temperatures were varied, while sintering in vacuum and parameters for best results concerning the highest sintered density were chosen. Results of the various sintering trials are shown in **Table 1**. It should be noted that these measured densities include the outer surface of samples, which was shown to be porous (**Figure 7**b) due to oxygen contamination, as demonstrated by EDX measurements.

While the sintering temperature only led to a minor increase in the density when going to the highest temperature of 1400 °C, the sintering time must be held for at least 210 min to reach a density of $4.19\,g\,cm^{-3}$ (corresponding to ≈93.16%) and above. A long sintering time and a high sintering temperature can lead to massive grain growth; therefore, a mean temperature and extended sintering, namely, 1350 °C for 5 h, were combined to create the highest sintering density while conserving a small grain size. Densities above 95% of the theoretical density (TD) of $4.5\,g\,cm^{-3}$ of CP titanium were repeatedly reached inside the bulk of the samples by applying this sintering schedule. These values lie well within the commonly reached densities when applying traditional sintering cycles.[29]

Controlled oxygen-free atmospheres are required for best densification to avoid the formation of oxides that would hinder sintering. Argon and vacuum sintering was therefore investigated for comparison of resulting densities and microstructures. Both atmospheres were successfully used to create sintering densities above $4.3\,g\,cm^3$, corresponding to 95% TD of pure titanium. BSE imaging (Figure 7) in a scanning electron microscope was used to investigate microstructural features created by the specific atmospheres. Both atmospheres develop significant surface layers (Figure 7b) that appear dark in BSE imaging due to the presence of lower atomic mass elements such as carbon and oxygen. The surface layers show a characteristic lamellar α-case structure caused by increased oxygen content.
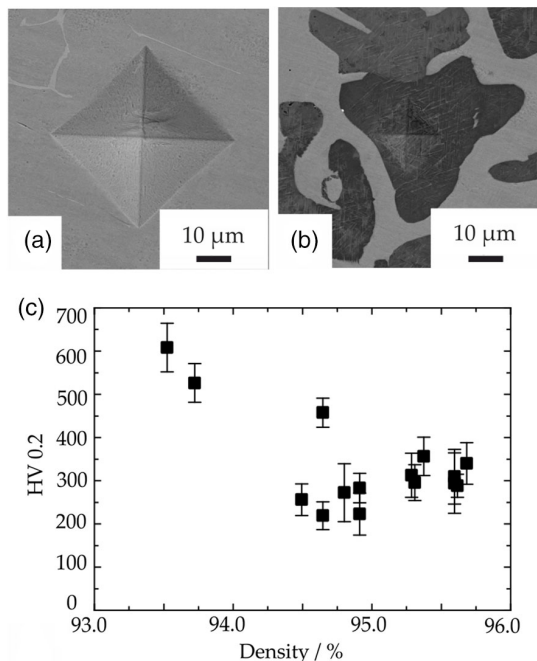
In addition, a higher amount of pores can be noted within these surface areas. The light matrix structure comprises α-Ti grains and contains darker regions visualizing elemental differences in the metal composition (Figure 7c). These phases contain a higher amount of light elements such as oxygen uptake from the remaining oxygen content inside the furnace and carbon emerging from binder degradation. As both O and C act as α-stabilizers, regions appearing darker in the element contrast are assigned to be secondary α-Ti. For both atmospheres, these regions within the bulk material and at the surface significantly increase the hardness caused by solid-solution strengthening (**Figure 8**).

NDIR-measured C content within the bulk material is 0.89 ± 0.03 wt% for the vacuum-sintered parts and 0.12 ± 0.02 wt% for the argon-sintered parts. These values indicate a more thorough polymer removal in the presence of argon gas flow. In contrast, O content was much lower for the parts sintered in vacuum with an amount of 0.56 ± 0.01 wt% in comparison with 1.52 ± 0.18 wt% after sintering in argon. Both trends agree with Shibo et al., who investigated the correlation between debinding atmosphere and carbon or oxygen uptake for powder-injection-molded (PIM) titanium alloy.[30] Microstructural investigations reveal significantly higher amounts of retained α-phase developed within the bulk metal for the argon-sintered samples, whereas the vacuum samples only show certain discrete regions of retained α-phase. The
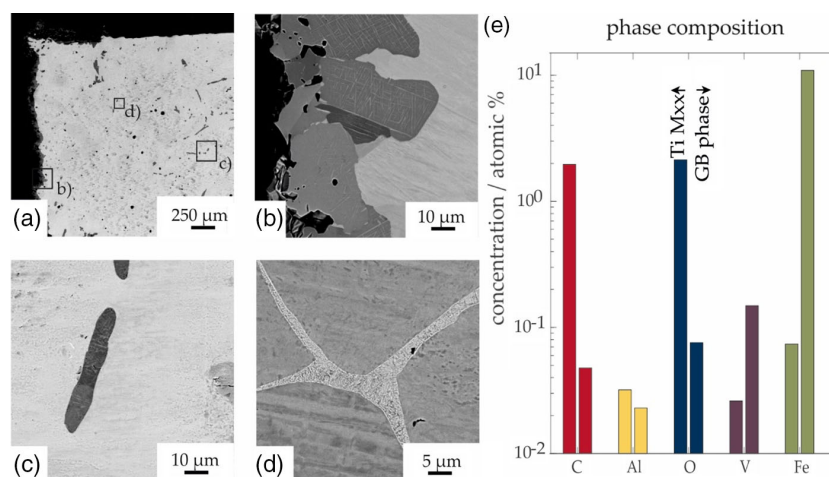
Figure 7. Microstructural features of titanium after debinding and sintering in vacuum atmosphere: a) overview of one corner of the sample of which images with higher magnifications were taken, b) clear α-phase case along the surface with an increased amount of larger pores, c) discrete region of retained α inside the bulk material, and d) lamellar α + β GB. e) Comparison of elemental concentrations of main trace elements in the GB phase and the matrix (Ti Mxx) analyzed by APT.

**ADVANCED
SCIENCE NEWS**

www.advancedsciencenews.com

**ADVANCED
ENGINEERING
MATERIALS**

www.aem-journal.com

Figure 8. Vickers indents a) in the α matrix phase and b) in the retained α-Ti phase corresponding to values of a) 295 $HV_{0.2}$ and b) 925 $HV_{0.2}$, respectively. c) The dependency of the hardness of the pure α-Ti matrix phase on the sintered density.

formation of α-Ti regions within the bulk material is induced by increased oxygen content.

While this retained α-phase is distributed inside the α grains, light regions along the grain boundaries show another particular microstructure. The light GB phase is either surrounded by darker regions or penetrated by dark lamellae, as shown in Figure 7d, creating a lamellar GB region. APT of the GB phase and the matrix reveals the compositional differences on the atomic scale. Concentrations of alloying elements are shown in Figure 7e) on a logarithmic scale. A clear Fe enrichment in the GB phase was identified, together with the depletion of C and O. Based on this analysis, the light contrast in the BSD image indicates enrichment of Fe at the GB that is contained as a trace element in the powder raw material and can accumulate due to enhanced diffusion along the grain boundaries. Consequently, the darker regions show depletion of Fe in nearby regions. As Fe acts as a β-Ti stabilizer, the GB phase conserves the body-centered cubic structure even after cooling down below the β transus temperature of 882 °C for pure titanium. If the Fe GB diffusion is strong and the local Fe concentration increases above 0.05 wt%, the microstructure undergoes an α-Ti+β-Ti two-phase region during cooling, leading to a formation of lamellar structures (Figure 7d). This β formation along the grain boundaries of α-Ti grains was also observed by Yan et al.[20] and is the expectable microstructure for sintered CP titanium. Both the β-Ti phases and the secondary α-regions appear in the vacuum and argon-sintered samples; however, they are much more pronounced for the argon parts. This microstructure agrees with prior studies on sintering of titanium, which revealed lower final density and higher impurity levels if argon was used as the sintering atmosphere.[30]

According to Bin et al., the amount of oxygen solid-solution hardening in pure titanium powder materials can be calculated as 287.9 HV mass%$^{-1}$.[18] Therefore, an increase in hardness of 161 HV emerging from 0.56 wt% oxygen in the vacuum sintering case can be calculated. Starting at 120 HV for CP titanium, the resulting hardness would be expected to be 281 HV.

The measured hardness of the matrix material of the vacuum-sintered samples lies at 258 ± 36 $HV_{0.2}$ (if >95% TD is achieved) (Figure 8c). It is noteworthy that this value is gradually increased if measuring within a region of 300 μm to the surface, where a mean value of 310 ± 53 $HV_{0.2}$ was determined. The hardness of the matrix α-Ti correlates strongly with the density of the sintered material. A lower density indicates reduced sintering activity in these samples and is the result of increased oxygen uptake during processing. A comparison of samples that were sintered after compression with samples that were not compressed in the green state shows significantly higher oxygen uptake without compression. The difference is due to a reduction in open pore surface area as a result of compression, which reduces diffusion pathways for oxygen. Accordingly, a reduction in porosity in the green state reduces oxidation of the particle surfaces and results in a higher sintered density. Without compression, the resulting higher oxygen content causes strong solid-solution strengthening and increased hardness at lower densities, as shown in Figure 8 and in **Table 2**.

The secondary α-Ti regions, appearing mainly on the surface, induced by an increased amount of oxygen consequently, show much higher hardness of 900 $HV_{0.2}$ and above. This hardness agrees with the combined hardening effects of the oxygen and carbon contents in the bulk material.

The increased amount of impurities and the remaining porosity after sintering lead to an increase in the hardness of the obtained titanium. The assumed hardness of 120 HV[31] for CP titanium cannot be achieved after sintering but rather almost the triple value. Nonetheless, the hardness of the bulk matrix material lies in the same range as for CP titanium that was additively manufactured by SLM.[32]

3.4. Tensile Tests

Microtensile tests were conducted to quantify the mechanical strength of sintered titanium parts. **Figure 9**a shows representative stress−strain curves of printed and vacuum-sintered samples and a conventionally fabricated CP Ti sheet as reference

Table 2. Summary of properties of sintered MF^3 titanium specimen.

Properties of sintered MF^3 specimen			
	Relative density [%]	Hardness [HV0.2]	O2 content [wt%]
Uncompressed 1	93.5	608 ± 56	1.65 ± 0.14
Uncompressed 2	93.7	526 ± 45	1.66 ± 0.16
Compressed 1	94,5	256 ± 37	0.56 ± 0.01
Compressed 2	94,6	219 ± 32	0.54 ± 0.03
Compressed 3	95,7	340 ± 48	0.46 ± 0.02
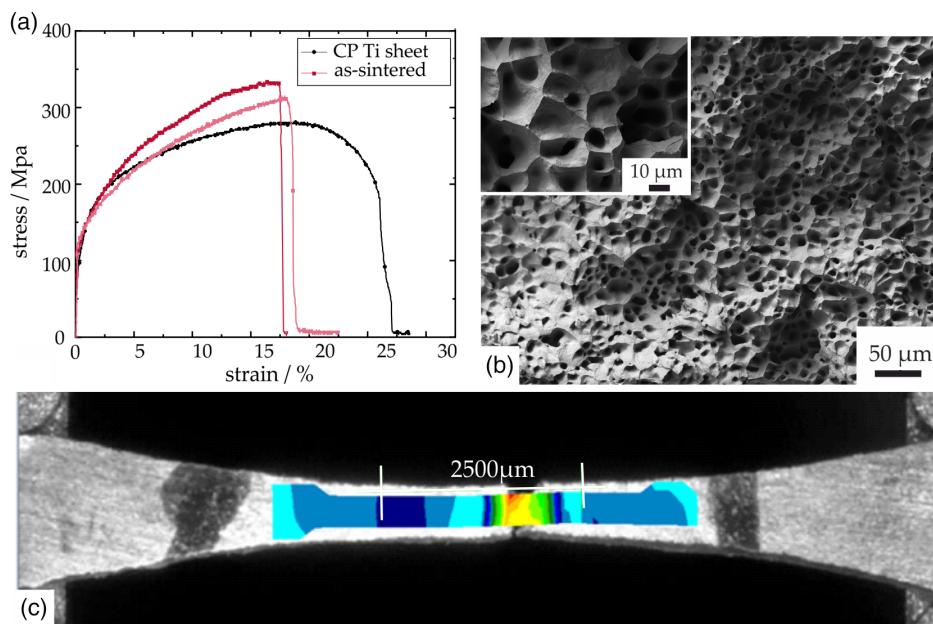
Figure 9. Results of microtensile testing: a) stress–strain curves of sintered and conventional rolled CP titanium, b) fractured surfaces of sintered samples, and c) deformed sample at the end of the measurement. The overlying colors in (c) indicate regions of highest strain.

material. Elongations were calculated using the effective gauge length derived from regions of highest elongations, as shown in Figure 9c, by digital image correlation.

Higher strength at a reduced elongation of sintered samples can be stated compared with rolled and annealed CP titanium sheet material. The increase in strength correlates well with the already measured increased hardness of the sintered titanium, emerging from impurity uptake during high-temperature processing. Nonetheless, the measured hardness values in the range of 300 $HV_{0.2}$ indicate strength values significantly higher than the measured 350 MPa, which should rather lie in the range of 700 MPa.[14] Comparable SLM CP titanium with similar hardness displayed an ultimate tensile strength above 750 MPa.[32] The reduced elongation is a result of premature fracture after reaching uniform elongation. The SEM images of the fractured specimen (Figure 9b) reveal pore opening under the applied tensile stress that leads to fractioning due to the layered character of the printed samples. The typical dimples on the fractured surface indicate that the fracture mode was a ductile fracture and the fracture mechanism was microporous aggregation. This porosity contributes to a decline in the final strength of sintered samples and erases the solid-solution strengthening of impurities. However, the reduction in ductility resulting from solid-solution hardening is still valid and is likely to intensify the decrease in elongation caused by the remaining porosity. Hence, for satisfying elongations, the O content of titanium and titanium alloys should be below 0.3 wt%.[13] The obtained elongations with values around 17 % are comparable with CP titanium fabricated by PIM[13,14] but are significantly reduced compared with conventionally fabricated CP titanium.[31] Therefore, apart from reducing impurity uptake during thermal treatments, porosity and print-related defects should be further reduced for enhanced strength.

3.5. Electrochemical Behavior

To evaluate the electrochemical stability of as-sintered samples prepared in separate batches, an electrochemical protocol, as shown as a red curve in **Figure 10**a, was applied to each of the studied electrodes. It consists of a hold at the OCP followed by anodic sweep of potential (10 mV s^{-1}) up to a value of potential corresponding to the current density of 1 mA cm^{-2}. The concentration of dissolved Ti in the electrolyte was monitored online by SFC–ICP–MS (Figure 10b). The recorded current response versus potential is shown in Figure 10c to facilitate the interpretation of the electrochemical data. Both samples dissolve during the initial contact with electrolyte at OCP (Figure 10b). Such initial dissolution is observed for most of the metals in contact with the electrolyte media and corresponds to either corrosion of the metal itself or dissolution of some metastable oxide phases present on the surface of the samples.[32]

Samples from different batches differ in the amount of initially dissolved Ti. This difference might be attributed to the various components in the surface oxides formed on these samples, as the formation of such phases strongly depends on the external conditions, such as room temperature, humidity, and duration of contact with air. The decrease in the initial dissolution with time indicates stabilization of the surfaces. During the potential sweep in the anodic direction, the dissolution of Ti increases for both of the samples. In these conditions, dissolution coincides with several processes, such as the transformation of the film to a more stoichiometric oxide and the oxygen evolution reaction, which induces degradation. Similar to the initial dissolution behavior, the samples produced in different batches also differ under the anodic sweep of potential, as shown in both Ti dissolution rates and polarization curves. Moreover, samples
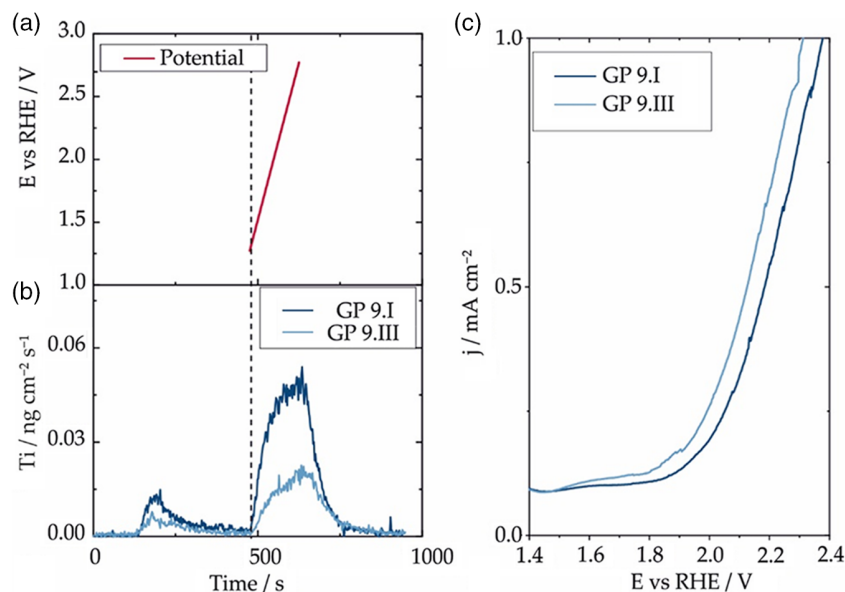
Figure 10. Electrochemical behavior of as-sintered Ti samples produced in different batches. a) Applied potential; b) Ti dissolution profiles; and c) anodic polarization curves obtained at the scan rate of $10\,mV\,s^{-1}$. Electrolyte: Ar-saturated 0.1 M $HClO_4$.

of different batches show different abilities to form oxide films, as indicated by the difference in the plateau current of the polarization curves in Figure 10c.

Summarized dissolution data for the samples produced in different batches are shown in **Table 3**. The dissolution of Ti foil recorded under the same electrochemical protocol is also shown for comparison. The amounts of dissolved Ti are derived from the dissolution profiles by the integration of the dissolution peaks corresponding to the OCP conditions and the anodic sweeps. It is important to note that the amount of dissolved Ti from both samples is relatively low compared with conventionally used Ti, at both the OCP conditions and the oxygen evolution reaction. These results suggest that Ti prepared by MF^3 can be a promising material for electrochemical applications considering its enhanced stability toward dissolution even under the harsh conditions of the oxygen evolution reaction. In particular, MF^3 Ti can find application as bipolar plates on the anode side in the PEM electrolyzers or replace conventionally produced Ti in the preparation of dimensionally stable anodes for chlorine evolution, platinized titanium anodes used in electroplating, and electrosynthesis of potent oxidizing agents or water treatment.

Table 3. Summary of the electrochemical dissolution.

Sample[a]	Initial dissolution of Ti, ng cm^{-2}	Anodic dissolution of Ti, ng cm^{-2}
GP 9.I	11.5 ± 1.5	61.9 ± 3.6
GP 9.III	4 ± 0.8	26.3 ± 1.4
Ti foil	369.5 ± 15	160.2 ± 10

[a]The standard deviation was calculated based on the results of three identical measurements on different spots of the sample.

4. Conclusion

Additive manufacturing of titanium parts was successfully realized by application of the MF^3 process. Nominally dense printing, controlled thermal debinding with thorough removal of degradation products, and high sintering densification were identified as crucial parameters for the fabrication of titanium of high chemical purity and satisfying mechanical performance. The shaping of green bodies was thereby optimized by adjusting extrusion temperature and infill patterns during the printing of highly filled filaments. Additional consolidation of green bodies was obtained by warming to 180 °C and compression at 92 MPa, leading to the closure of minor printing defects. During thermal debinding, slow heating rates and oxygen-free furnace atmospheres became decisive for polymer removal and conservation of sample shape. Constant argon flow provided carbon removal, whereas the oxygen uptake could be better prevented in vacuum levels of 10^{-4} mbar.

Consequently, the microstructure of vacuum-sintered samples contains less-retained α and Fe-enriched GB regions than argon samples. This microstructure also influences the tensile properties, leading to high strength at reduced ductility due to remaining porosity. Overall, the chemical purity of the printed and sintered samples lies in a satisfying range despite significantly increased oxygen content. By improving vacuum levels, the oxygen content in the sintered titanium could still be reduced, which would contribute to a more homogeneous microstructure and enhanced tensile properties.

The sintered titanium samples show slightly different electrochemical performance, which might be attributed to the different composition and state of their surfaces. Relatively high stability was proven by low amounts of dissolved Ti with anodic dissolution in the range of 25–60 ng cm^{-2}. This electrochemical behavior makes the additively manufactured titanium suitable for

electrochemical applications such as titanium bipolar plates for anode sides.

Conflict of Interest

The authors declare no conflict of interest.

Data Availability Statement

Research data are not shared.

[1] T. Hottinen, M. Mikkola, T. Mennola, P. Lund, *J. Power Sources* **2003**, *118*, 183.

[2] M. T. Mohammed, V. G. Semelov, A. V. Sotov, *Mater. Res. Express.* **2020**, *6*, 122006.

[3] L.-C. Zhang, Y. Liu, S. Li, Y. Hao, *Adv. Eng. Mater.* **2018**, *20*, 1700842.

[4] F. Wang, S. Williams, P. Colegrove, A. A. Antonysamy, *Metall. Mater. Trans. A.* **2013**, *44*, 968.

[5] P. Satish Kumar, L. Suvarna Raju, L. Siva Rama Krishna, *Int. Conf. Emerg. Trends Eng. ICETE*, Learning and Analytics in Intelligent Systems, vol. 2 (Eds: S. Satapathy, K. Raju, K. Molugaram, A. Krishnaiah, G. Tsihrintzis, Springer, Cham **2020**, pp. 587–600, https://doi.org/10.1007/978-3-030-24314-2_70.

[6] M. Vaezi, P. Drescher, H. Seitz, *Materials* **2020**, *13*, 922.

[7] E. Wheat, M. Vlasea, J. Hinebaugh, C. Metcalfe, *Mater. Des.* **2018**, *156*, 167.

[8] P. Singh, V. K. Balla, A. Gokce, S. V. Atre, K. H. Kate, *Prog. Addit. Manuf.* **2021** https://doi.org/10.1007/s40964-021-00167-5.

[9] A. Amherd Hidalgo, R. Frykholm, T. Ebel, F. Pyczak, *Adv. Eng. Mater.* **2017**, *19*, 1600743.

[10] Y. Zhang, S. Bai, M. Riede, E. Garratt, A. Roch, *Addit. Manuf.* **2020**, 101256.

[11] P. Singh, V. K. Balla, S. V. Atre, R. M. German, K. H. Kate, *Powder Technol.* **2021**, *386*, 9.

[12] F04 Committee, *ASTM F67-13, Standard Specification For Unalloyed Titanium, For Surgical Implant Applications (UNS R50250, UNS R50400, UNS R50550, UNS R50700)*, ASTM International, West Conshohocken, PA, **2013**. https://doi.org/10.1520/F0067-13.

[13] T. Ebel, V. Friederici, P. Imgrund, T. Hartwig, *Titan. Powder Metall.* **2015**, 337.

[14] R. M. German, *Powder Inject. Mold. Int.* **2009**, *3*, 4.

[15] K. Akechi, Z. Hara, *Powder Metall* **1981**, *24*, 41.

[16] M. Qian, G. B. Schaffer, C. J. Bettles, *Sinter. Adv. Mater.* **2010**, 324.

[17] F. H. Froes, O. N. Senkov, J. I. Qazi, *Int. Mater. Rev.* **2004**, *49*, 227.

[18] S. Bin, L. Shufeng, L. Hisashi, U. Junko, K. Katsuyoshi, *Trans. JWRI* **2012**, *41*, 1.

[19] J. D. Paramore, Z. Z. Fang, M. Dunstan, P. Sun, B. G. Butler, *Sci. Rep.* **2017**, *7*, 41444.

[20] M. Yan, S. D. Luo, G. B. Schaffer, M. Qian, *Metall. Mater. Trans. A.* **2013**, *44*, 3961.

[21] J. Gonzalez-Gutierrez, S. Cano, S. Schuschnigg, C. Kukla, J. Sapkota, C. Holzer, *Materials*, **2018**, *11*, 840.

[22] W. Lengauer, I. Duretek, M. Fürst, V. Schwarz, J. Gonzalez-Gutierrez, S. Schuschnigg, C. Kukla, M. Kitzmantel, E. Neubauer, C. Lieberwirth, V. Morrison, *Int. J. Refract. Met. Hard Mater.* **2019**, *82*, 141.

[23] J. Gonzalez-Gutierrez, F. Arbeiter, T. Schlauf, C. Kukla, C. Holzer, *Mater. Lett.* **2019**, *248*, 165.

[24] Y. Thompson, J. Gonzalez-Gutierrez, C. Kukla, P. Felfer, *Addit. Manuf.* **2019**, *30*, 100861.

[25] T. Li, J. Gonzalez-Gutierrez, I. Raguž, C. Holzer, M. Li, P. Cheng, M. Kitzmantel, L. Shi, L. Huang, *Addit. Manuf.* **2021**, *37*, 101700.

[26] C. Kukla, J. Gonzalez-Gutierrez, I. Duretek, S. Schuschnigg, C. Holzer, in *AIP Conf. Proc.* **2017**, *1914*, 190006, https://doi.org/10.1063/1.5016795.

[27] J. Gonzalez-Gutierrez, D. Godec, C. Kukla, T. Schlauf, C. Burkhardt, C. Holzer, in *16th Int. Sci. Conf. Prod. Eng. - Computer Integrated Manufacturing and High Speed Machining*, Vol. 16, Zadar, Croatia **2017**.

[28] A. A. Topalov, I. Katsounaros, M. Auinger, S. Cherevko, J. C. Meier, S. O. Klemm, K. J. J. Mayrhofer, *Angew. Chem. Int. Ed.* **2012**, *4*.

[29] R. M. German, *Int. J. Refract. Met. Hard Mater.* **2020**, *89*, 105214.

[30] G. Shibo, Q. Xuanhui, H. Xinbo, D. Ting, D. Bohua, *J. Mater. Process. Technol.* **2006**, *173*, 310.

[31] ASM Material Data Sheet, http://asm.matweb.com/search/SpecificMaterial.asp?bassnum=mtu010, (accessed March, 2020).

[32] H. Attar, M. Calin, L. C. Zhang, S. Scudino, J. Eckert, *Mater. Sci. Eng. A.* **2014**, *593*, 170.